GEOPHYSICS, VOL. 85, NO. 2 (MARCH-APRIL 2020); P. R101–R111, 17 FIGS.
10.1190/GEO2019-0285.1

Check for updates

Downloaded 04/29/20 to 73.78.60.103. Redistribution subject to SEG license or copyright; see Terms of Use at http://library.seg.org/

# Elastic full-waveform inversion with probabilistic petrophysical model constraints

Odette Aragao[1] and Paul Sava[1]

## ABSTRACT

Full-waveform inversion (FWI) based on the minimization of data residuals may not enhance our understanding of the subsurface and can at times lead to misleading subsurface models. Additionally, unconstrained multiparameter FWI may also lead to models that do not represent realistic lithology for independently derived parameters. We have developed a method for elastic FWI that explicitly imposes petrophysical restrictions to guide models toward realistic and feasible lithology, that is, to subsurface models consistent with the seismic data and with the underlying petrophysics. We exploit petrophysical information, such as that provided by well logs, to constrain the inversion and to avoid implausible models. We achieve this goal by confining the inverted models to a feasible region defined by a probability density function instead of imposing lithologic facies as a function of position. Inside this feasible petrophysical regime, the inverted models do not need to obey a specific trend, that is, we do not link the parameters with explicit and potentially inaccurate petrophysical relations. Instead, we define a petrophysical basin of attraction that confines models to a feasible region validated by regional lithologic and petrophysical information. We find through elastic models that incorporating probabilistic petrophysical constraints into the inversion objective function leads to models that are superior to models obtained either without constraints or with approximate analytic constraints. In addition, we discover that these constraints can help in mitigating common issues affecting elastic FWI, such as the artifacts produced by interparameter crosstalk and limited acquisition coverage.

## INTRODUCTION

One of the greatest challenges in seismic exploration consists of estimating accurate subsurface elastic models. Seismic tomography is becoming a standard technique for subsurface imaging at various scales, and it aims to build high-resolution models of the physical parameters underlying the wave propagation. The main approaches to seismic tomography use either traveltimes (Woodward, 1992; Schuster and Quintus-Bosz, 1993; Taillandier et al., 2009; Djebbi and Alkhalifah, 2018) or wavefields (Tarantola, 1984; Mora, 1989; Biondi, 2006; Duan and Sava, 2016; Diaz and Sava, 2017). Wavefield tomography has advantages over traveltime tomography because it recovers parameters with higher resolution (Tarantola, 1986; Pratt, 1999; Operto et al., 2013; Alkhalifah and Choi, 2014) by exploiting the kinematics and dynamics of the observed waveforms.

Full-waveform inversion (FWI) is among the most promising techniques in the wavefield tomography category because it delivers highly accurate subsurface models from seismic data (Tarantola, 1984; Pratt, 1999; Sirgue and Pratt, 2004; Virieux and Operto, 2009). FWI operates by iteratively updating model parameters based on the mismatch between observed and simulated data. This optimization exploits seismic wavefield modeling (the forward problem) and solves the associated inverse problem by minimizing an objective function. The gradient of the objective function estimates model perturbations that progressively decrease the data residual. Conventional FWI implementations use the adjoint-state method (Plessix, 2006) to compute the objective function gradient because this method is among the most efficient and requires the least amount of storage.

Early implementations of FWI used the acoustic wave equation (Tarantola, 1984; Pratt, 1990; Pratt et al., 1996). However, acoustic FWI does not take into account elastic effects and the presence of S-waves in the data. Several parameters are necessary for describing

Manuscript received by the Editor 3 May 2019; revised manuscript received 5 December 2019; published ahead of production 30 December 2019; published online 27 February 2020.
[1]Colorado School of Mines, Center for Wave Phenomena, Department of Geophysics, Golden, Colorado 80401, USA. E-mail: aquinodearagao@mines.edu (corresponding author); psava@mines.edu.
© 2020 Society of Exploration Geophysicists. All rights reserved.

Downloaded 04/29/20 to 73.78.60.103. Redistribution subject to SEG license or copyright; see Terms of Use at http://library.seg.org/

elastic models (e.g., density $\rho$ and Lamé parameters $\lambda$ and $\mu$ or density and P- and S-wave velocities). Therefore, elastic FWI (EFWI) better describes the subsurface properties (Tarantola, 1988; Pratt, 1990; Plessix, 2006; Oh et al., 2018; Zhang et al., 2019).

Despite its popularity, FWI is hampered by several challenges undermining its practical application. FWI is a highly nonlinear and ill-posed problem, so its convergence is subjected to falling into local minima (Symes, 2008; Virieux and Operto, 2009). Therefore, one needs to include prior information into inversion to find a plausible solution (Tikhonov and Arsenin, 1977; Tarantola, 2005). Also, the wave extrapolator can become unstable when model updates fluctuate, thus impending further updates.

EFWI suffers from several additional practical difficulties. First, using multiple parameters increases the degrees of freedom in the model space, thereby increasing the nonlinearity of the inversion (Operto et al., 2013). In addition, because the model parameters are updated simultaneously but independently, different model components can be physically contradictory to one another, creating combinations that are lithologically implausible or impossible. This situation may create inaccurate and unstable forward solutions and lead to poor convergence (Baumstein, 2013). Moreover, similar radiation patterns among various elastic parameters create crosstalk; that is, different models are viewed similarly in data (Operto et al., 2013; Kamath and Tsvankin, 2016) resulting in ambiguous model inversion. Radiation pattern analysis can partially correct for crosstalk, but it is largely ineffective in poorly illuminated areas.

To recover models that are self-consistent and properly characterize the subsurface, we need to explicitly impose model constraints during the inversion (Baumstein, 2013; Duan and Sava, 2016; Manukyan et al., 2018; Rocha and Sava, 2018; Zhang et al., 2018). These constraints can use petrophysical information, such as that contained in well logs or from other sources, such as core or basin analysis. Incorporating constraints into the objective function defines the model space bounds, forcing the inverted models to be consistent with known petrophysical relationships and thus represent realistic lithologic units.

Baumstein (2013) uses projection onto convex sets to incorporate constraints into acoustic FWI. These constraints impose velocity bounds (box constraints) and specify a minimum smoothness for the model parameters. The updated models must be at the intersection of all convex sets, which leads to more stable simulations and a geologically plausible structure. Manukyan et al. (2018) constrain the inversion by assuming that the elastic parameters have structural similarity and thus mitigate parameter trade-off problems and the different spatial resolution of elastic parameters. They show that structurally constrained FWI can deliver higher quality models when compared with conventional FWI. However, the assumption of structural similarity between different elastic parameters can potentially compromise the final outcome. Zhang et al. (2018) and Zhang and Alkhalifah (2019) use seismic facies to build a model regularization term for EFWI to deliver more reliable models. Zhang et al. (2018) update the distribution of the facies at each iteration using a Bayesian approach, whereas Zhang and Alkhalifah (2019) estimate the facies distribution by training deep neural networks.

Duan and Sava (2016) use a logarithmic penalty function to constrain the elastic wavefield tomography assuming a general linear relationship between the model parameters. Rocha and Sava (2018) also use this type of constraint, but in the context of elastic reflection waveform inversion. Both examples demonstrate that an explicit petrophysical constraint can yield consistent and plausible models even if conventional spatial regularization is not explicitly applied during the inversion. However, complex models do have nonlinear petrophysical relationships between the elastic parameters. Moreover, the analytic logarithmic barrier constraint works with user-defined parameters, and their selection may be challenging, especially when different lithofacies are present in the same area. Thus, it is necessary to define more general and automated petrophysical constraints that provide flexibility and adapt to the specific geologic situation in the imaged area.

We propose elastic wavefield tomography with an objective function that constrains the relationship between the elastic parameters using probability density functions (PDFs) (Aragao and Sava, 2019). In the following sections, we first discuss general aspects of EFWI, emphasizing the mechanisms used to incorporate constraints into the inversion. We demonstrate that PDFs can be used in EFWI without knowing or defining an analytic relationship among the different elastic parameters. Finally, we illustrate the features and performance of the proposed method with two synthetic examples.

## ELASTIC WAVEFIELD TOMOGRAPHY

In this section, we discuss the basis of EFWI and introduce the framework for probabilistic petrophysical model constraints.

We consider the isotropic elastic wave equation

$$\rho\ddot{\mathbf{u}} - \lambda[\nabla(\nabla\cdot\mathbf{u})] - \mu[\nabla\cdot(\nabla\mathbf{u}+\nabla\mathbf{u}^T)] = \mathbf{f}, \quad (1)$$

where $\mathbf{u}(e,\mathbf{x},t)$ is the elastic wavefield; $\mathbf{f}(e,\mathbf{x},t)$ is the source function; $\lambda(\mathbf{x})$ and $\mu(\mathbf{x})$ are the Lamé parameters; $\rho(\mathbf{x})$ is the density; and $e$, $\mathbf{x}$, and $t$ are, respectively, the experiment index, space coordinates, and time. Equation 1 assumes that the Lamé parameters vary slowly, such that their spatial gradient can be neglected.

Considering $\mathbf{u}_s$ as the source wavefield, the waveform inversion problem is solved by minimizing an objective function $\mathcal{J}(\mathbf{u}_s,\lambda,\mu)$ consisting of three parts: a term that evaluates the misfit between the simulated and observed data, $\mathcal{J}_D(\mathbf{u}_s,\lambda,\mu)$; a model regularization term, $\mathcal{J}_M(\lambda,\mu)$, that enforces spatial correlation of the model parameters; and a term that enforces the petrophysical model constraints, $\mathcal{J}_C(\lambda,\mu)$:

$$\mathcal{J}(\mathbf{u}_s,\lambda,\mu) = \mathcal{J}_D(\mathbf{u}_s,\lambda,\mu) + \mathcal{J}_M(\lambda,\mu) + \mathcal{J}_C(\lambda,\mu). \quad (2)$$

We can define the data residual

$$\mathbf{r}_D(e,\mathbf{x},t) = \mathbf{W}_u(e,\mathbf{x},t)\mathbf{u}_s(e,\mathbf{x},t) - \mathbf{d}_{\text{obs}}(e,\mathbf{x},t) \quad (3)$$

and then the data misfit term

$$\mathcal{J}_D(\mathbf{u}_s,\lambda,\mu) = \sum_e \frac{1}{2}\|\mathbf{r}_D(e,\mathbf{x},t)\|^2, \quad (4)$$

where $\mathbf{W}_u(e,\mathbf{x},t)$ are the weights that restrict the source wavefield $\mathbf{u}_s(e,\mathbf{x},t)$ to the known receiver locations and $\mathbf{d}_{\text{obs}}(e,\mathbf{x},t)$ are the observed data.

To update the model iteratively using a gradient-based method (Tarantola, 1988), one can compute the gradient of $\mathcal{J}_D$ with respect to the model parameters $\lambda$ and $\mu$ using the adjoint-state method (Plessix, 2006). This method consists of four steps:

Downloaded 04/29/20 to 73.78.60.103. Redistribution subject to SEG license or copyright; see Terms of Use at http://library.seg.org/

1) Compute the seismic wavefield $\mathbf{u}_s(e,\mathbf{x},t)$ from a source function $\mathbf{f}_s$, such that $\mathbf{L}\mathbf{u}_s - \mathbf{f}_s = \mathbf{0}$, where $\mathbf{L}$ is the linear elastic wave operator derived from equation 1.
2) Compute the adjoint source $\mathbf{g}_s = \partial\mathcal{J}_D/\partial\mathbf{u}_s$, which exploits the difference between the observed and simulated data (equation 3).
3) Compute the adjoint wavefield $\mathbf{a}_s(e,\mathbf{x},t) = \mathbf{L}^T\mathbf{g}_s$, which uses the adjoint elastic wave operator $\mathbf{L}^T$.
4) Compute the gradient of $\mathcal{J}_D$ with respect to the parameters $\lambda$ and $\mu$ using

$$\begin{bmatrix} \frac{\partial\mathcal{J}_D}{\partial\lambda} \\ \frac{\partial\mathcal{J}_D}{\partial\mu} \end{bmatrix} = \sum_e \begin{bmatrix} -\nabla(\nabla\cdot\mathbf{u})\star\mathbf{a}_s \\ -\nabla(\nabla\mathbf{u}+\nabla\mathbf{u}^T)\star\mathbf{a}_s \end{bmatrix}, \tag{5}$$

where symbol $\star$ represents the zero-lag time crosscorrelation.

Incorporating a model regularization term into the objective function may reduce the inversion ill-posedness and accelerates convergence toward the global minimum (Asnaashari et al., 2013; Jun et al., 2017; Masmoudi and Alkhalifah, 2018; Zhang et al., 2018). Prior information can be estimated from nonseismic data, for example, well logs, or by incorporating knowledge about the model geometry, for example, smoothness or consistency with a migrated image. Considering the model residuals

$$\mathbf{r}_\lambda(\mathbf{x}) = \mathbf{W}_\lambda(\mathbf{x})(\lambda(\mathbf{x}) - \bar{\lambda}(\mathbf{x})) \tag{6}$$

and

$$\mathbf{r}_\mu(\mathbf{x}) = \mathbf{W}_\mu(\mathbf{x})(\mu(\mathbf{x}) - \bar{\mu}(\mathbf{x})), \tag{7}$$

the term $\mathcal{J}_M(\lambda,\mu)$ is

$$\mathcal{J}_M(\lambda,\mu) = \frac{1}{2}\|\mathbf{r}_\lambda(\mathbf{x})\|^2 + \frac{1}{2}\|\mathbf{r}_\mu(\mathbf{x})\|^2, \tag{8}$$

where $\bar{\lambda}(\mathbf{x})$ and $\bar{\mu}(\mathbf{x})$ are the prior (reference) models. The weighting operators $\mathbf{W}_\lambda(\mathbf{x})$ and $\mathbf{W}_\mu(\mathbf{x})$ are related to the model covariance matrices such that $\mathbf{W}_\lambda = \mathbf{C}_\lambda^{-1/2}$ and $\mathbf{W}_\mu = \mathbf{C}_\mu^{-1/2}$.

The gradient of $\mathcal{J}_M(\lambda,\mu)$ with respect to the model parameters $\lambda$ and $\mu$ is

$$\begin{bmatrix} \frac{\partial\mathcal{J}_M}{\partial\lambda} \\ \frac{\partial\mathcal{J}_M}{\partial\mu} \end{bmatrix} = \begin{bmatrix} \mathbf{W}_\lambda^T\mathbf{W}_\lambda(\lambda-\bar{\lambda}) \\ \mathbf{W}_\mu^T\mathbf{W}_\mu(\mu-\bar{\mu}) \end{bmatrix}. \tag{9}$$

It is apparent from equations 5 and 9 that the model components $\lambda$ and $\mu$ for multiparameter inversion are updated independently and thus can become physically inconsistent with each other, producing inaccurate models, inaccurate images, and inaccurate geologic interpretation. Explicitly incorporating petrophysical constraints improves the quality of the inversion by restricting the updated models to a feasible region, resulting in more accurate subsurface characterization.

Duan and Sava (2016) propose a logarithmic penalty function $\mathcal{J}_L$ to constrain the inversion to a feasible region by enforcing physical relationships between the updated model parameters:

$$\mathcal{J}_L(\lambda,\mu) = -a\sum_{\mathbf{x}}[\log(h_u) + \log(h_l)]. \tag{10}$$

The scalar parameter $a$ determines the strength of the constraint term in the objective function, and $h_u$ and $h_l$ are the linear functions such that

$$h_u = -\lambda + c_u\mu + b_u \tag{11}$$

and

$$h_l = \lambda - c_l\mu - b_l. \tag{12}$$

The coefficients $c_u$ and $c_l$ are the slopes of the boundary lines, and $b_u$ and $b_l$ are their intercepts. At the two linear boundaries of the feasible region

$$h_u = 0 \tag{13}$$

and

$$h_l = 0. \tag{14}$$

The term $\mathcal{J}_L$ forces the recovered models to the interior of a feasible region, that is, between the upper and lower boundaries, where $h_u$ and $h_l$ are positive. Outside this feasible region, $h_u$ and $h_l$ are negative; thus, the constraint term given in equation 10 prevents undesirable model updates. The distance of a given model parameter in the parameter space $\{\lambda,\mu\}$ to the boundary lines $h_u$ and $h_l$ determines the value of $\mathcal{J}_L$, such that this term dominates the objective function when models are close to either one of the barriers. This constraint forces the inverted models to move away from those boundaries, which acts like a barrier that favors model parameters in a given feasible region.

The gradient of $\mathcal{J}_L$ with respect to the model parameters $\lambda$ and $\mu$ is

$$\begin{bmatrix} \frac{\partial\mathcal{J}_L}{\partial\lambda} \\ \frac{\partial\mathcal{J}_L}{\partial\mu} \end{bmatrix} = a\begin{bmatrix} \frac{-1}{\lambda - c_u\mu - b_u} - \frac{1}{\lambda - c_l\mu - b_l} \\ \frac{c_u}{\lambda - c_u\mu - b_u} + \frac{c_l}{\lambda - c_l\mu - b_l} \end{bmatrix}. \tag{15}$$

The term $\mathcal{J}_L$ assumes that the relationship between the model parameters $\lambda$ and $\mu$ is linear. Therefore, the inversion may not be able to recover complex, nonlinear true physical relationships between the model parameters. Alternatively, if we have access to petrophysical information obtained, for example, from well logs, we can impose a more general kind of petrophysical constraint. In this situation, we can construct a PDF of the reference well-log parameters to characterize the interdependence between the elastic model parameters.

Consider, for example, the crossplot in Figure 1a illustrating a possible petrophysical relationship between the Lamé parameters $\lambda$ and $\mu$. The linear barrier constraint $\mathcal{J}_L$ would not be appropriate for this example because $\lambda$ and $\mu$ do not share a linear relationship. Instead, we can create a PDF (Figure 1b) based on the available values of $\lambda$ and $\mu$.

Considering the vector $\mathbf{m} = [\lambda\ \mu]$ as the elastic model components of a given position $\mathbf{x}$, we evaluate distances to all points of the PDF, represented by coordinates $\mathbf{p} = [\lambda_p\ \mu_p]$. For any given model represented by $\mathbf{m} = [\lambda\ \mu]$, we would like to evaluate a model space distance to the entire distribution (Figure 2). The distance between a given $\mathbf{m}$ to a point of coordinates $\mathbf{p}$ is

$$d(\mathbf{m},\mathbf{p}) = \|\mathbf{m}-\mathbf{p}\|_2. \tag{16}$$

Then, considering the probability density of each cell of the PDF as $f(\mathbf{p})$, we determine the distance $D(\mathbf{m})$ from $\mathbf{m}$ to the distribution as

$$\frac{1}{D(\mathbf{m})} = \sum_{\mathbf{p}} \frac{f(\mathbf{p})}{d(\mathbf{m},\mathbf{p})}. \tag{17}$$

Therefore, each point in the updated model space represented by $\mathbf{m}$ is connected to all cells of the PDF; that is, we have constructed a distance from this model to the distribution. Because the quantity $1/D(\mathbf{m})$ is small for points that are far from regions of high probability, we can define the petrophysical constraint $\mathcal{J}_P$ as

$$\mathcal{J}_P = a\sum_{\mathbf{m}} D(\mathbf{m}). \tag{18}$$

This definition imposes the condition that all points representing inverted models are as close as possible to the original petrophysical distribution without being drawn especially to any value of the model, but rather close in a statistical sense to the entire distribution. For stability, we explicitly exclude situations where the model space distance from $\mathbf{m}$ to a given $\mathbf{p}$ is equal to zero.

The gradients of $\mathcal{J}_P$ with respect to the model parameters $\lambda$ and $\mu$ are

$$\frac{\partial \mathcal{J}_P}{\partial \lambda} = aD^2(\mathbf{m})\sum_{\mathbf{p}} \frac{f(\mathbf{p})(\lambda-\lambda_p)}{d^3(\mathbf{m},\mathbf{p})} \tag{19}$$

and

$$\frac{\partial \mathcal{J}_P}{\partial \mu} = aD^2(\mathbf{m})\sum_{\mathbf{p}} \frac{f(\mathbf{p})(\mu-\mu_p)}{d^3(\mathbf{m},\mathbf{p})}. \tag{20}$$

Figure 1c displays the distribution of the gradient of $D(\mathbf{m})$, which is close to zero in the region where the PDF is high. The distance to high probabilities in the model parameter space defines the value of $\mathcal{J}_P$, such that the gradient of this term dominates in the total gradient of the objective function $\mathcal{J}$ if the updated models are far from high probability. Otherwise, once a point $\mathbf{m}$ in the updated model is consistent with the distribution given by the PDF, the data misfit $\mathcal{J}_D$ fully controls the gradient because the gradients of $\mathcal{J}_P$ are zero.

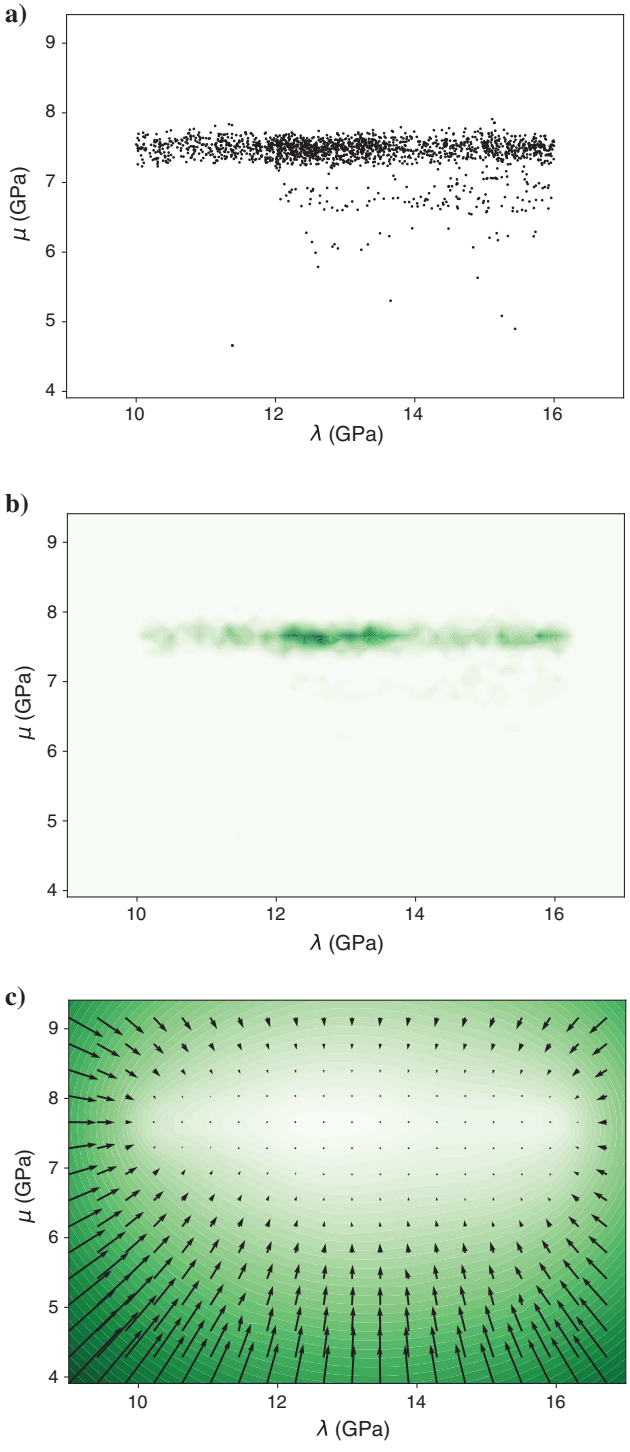


Figure 1. (a) Example of a $\lambda$ and $\mu$ crossplot. (b) PDF associated to the crossplot in (a), characterizing the dependence of $\lambda$ and $\mu$. (c) Distribution of the distance $D(\mathbf{m})$ and its gradient for the distribution shown in (b). Note that high-probability models are associated with small values of $D(\mathbf{m})$ and with zero gradients.

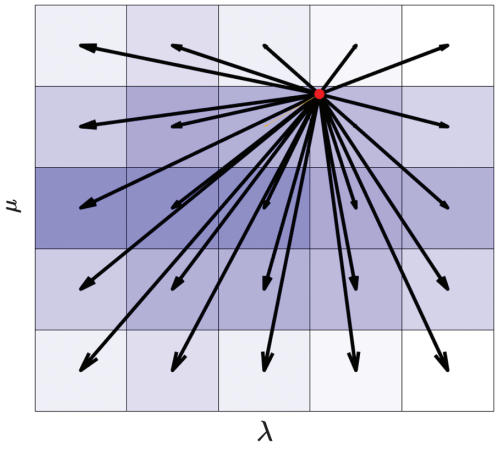


Figure 2. Sketch indicating how each point in the updated model space (the red dot) communicates with all cells of the PDF. Each cell of the PDF contributes proportionally with its probability value and inverse proportionally to the distance to the analyzed model.

Downloaded 04/29/20 to 73.78.60.103. Redistribution subject to SEG license or copyright; see Terms of Use at http://library.seg.org/

Downloaded 04/29/20 to 73.78.60.103. Redistribution subject to SEG license or copyright; see Terms of Use at http://library.seg.org/

The probabilistic petrophysical model constraint $\mathcal{J}_P$ addresses many issues related to EFWI. First, it can reduce the nonlinearity and the ill-posed nature of FWI because it incorporates prior information into the inversion, which reduces the number of model solutions and improves the inversion convergence to realistic and feasible inverted models, preventing instabilities in wavefield extrapolation. In addition, it avoids geologically implausible earth models and reduces the artifacts created by the interparameter crosstalk because it links the elastic parameters during the inversion and restricts them to a feasible region.

## EXAMPLES

We illustrate our EFWI method with two synthetic examples, and we compare inversions using only the data misfit term $\mathcal{J}_D$, the data misfit with the logarithmic penalty function $\mathcal{J}_D + \mathcal{J}_L$, and the data misfit with the probabilistic petrophysical constraints $\mathcal{J}_D + \mathcal{J}_P$. In the second example, we also repeat the inversion with the objection function $\mathcal{J}_D + \mathcal{J}_P$ for different choices of the trade-off parameter $a$, which determines the strength of $\mathcal{J}_P$ in the objective function.

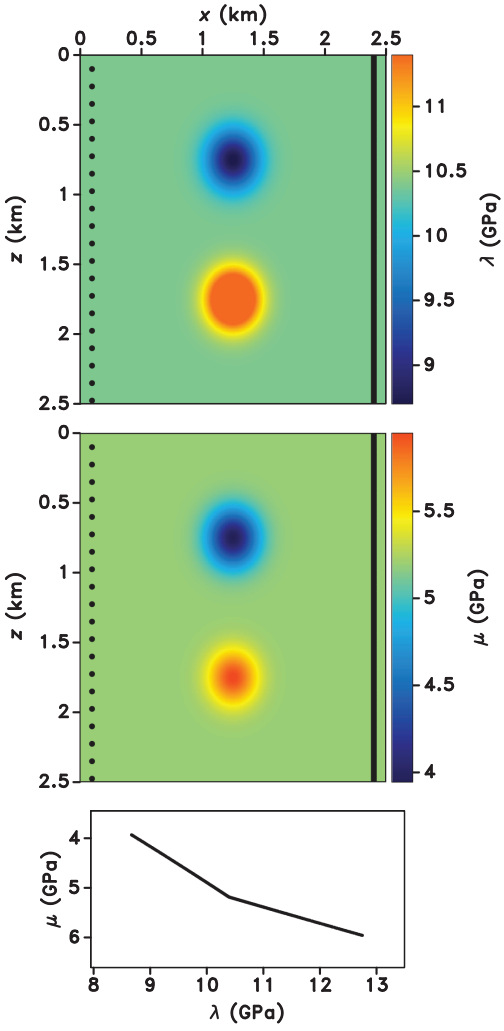


Figure 3. True $\lambda$ and $\mu$ models and their crossplot in the $\lambda$-$\mu$ space. The top panels show the sources (dots) located at $x = 0.1$ km, and the vertical line corresponds to receivers at $x = 2.4$ km. The negative and positive Gaussian anomalies for the $\lambda$ and $\mu$ models are centered at (1.25, 0.75) km and (1.25, 1.75) km, respectively. The crossplot shows two linear relationships between $\lambda$ and $\mu$, corresponding to each of the Gaussian anomalies.

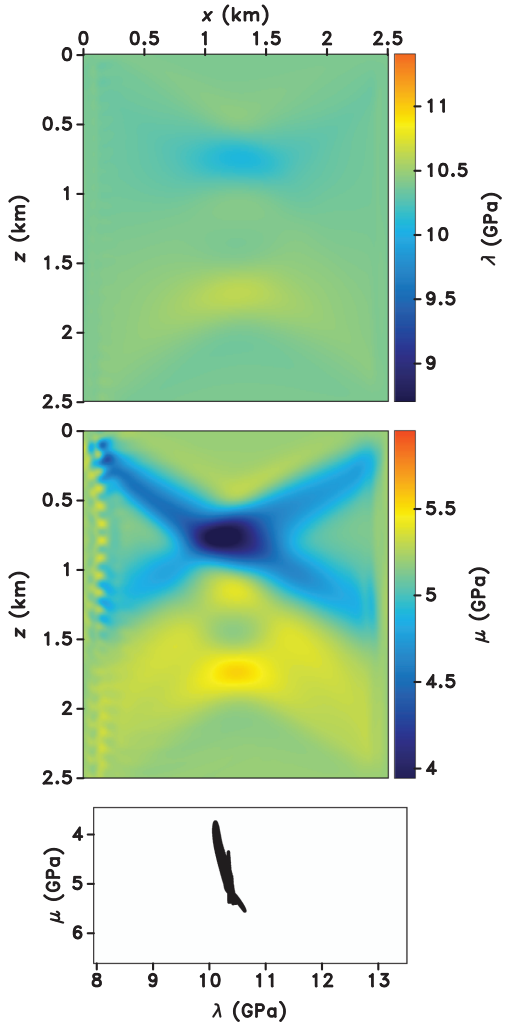


Figure 4. Updated $\lambda$ and $\mu$ models using the objective function $\mathcal{J}_D$. The Gaussian anomalies are not recovered well, and the inverted models present artifacts from interparameter crosstalk. The crossplot shows that the parameters do not follow the same trend of the true models (Figure 3).

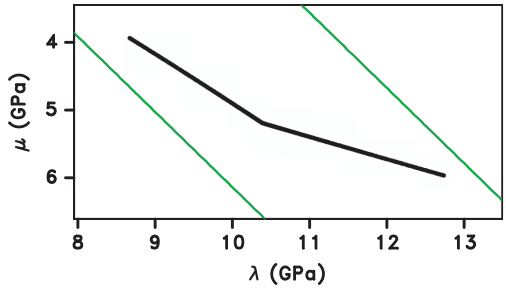


Figure 5. Crossplot in the $\lambda$-$\mu$ space of the true models superimposed by the upper and lower boundaries used in the logarithmic penalty function $\mathcal{J}_L$. The linear barriers ensure that the inversion recovers models confined to this feasible region.

Downloaded 04/29/20 to 73.78.60.103. Redistribution subject to SEG license or copyright; see Terms of Use at http://library.seg.org/

## Gaussian anomalies model

The first synthetic example uses a model with negative and positive Gaussian anomalies centered at (1.25, 0.75) and (1.25, 1.75) km, respectively (Figure 3). We simulate 20 vertical displacement sources in a well at $x = 0.1$ km and a line of geophones at $x = 2.4$ km. Figure 3 shows the true $\lambda$ and $\mu$ models along with a crossplot of the models. We choose this simple example to show how the inversion using a data misfit with the logarithmic penalty function fails when the model is characterized by two clusters, which represent lithologies with different linear relationships between parameters $\lambda$ and $\mu$. We initiate the inversion with constant backgrounds from the true models.

Figure 4 shows the recovered $\lambda$ and $\mu$ models using the objective function $\mathcal{J}_D$ along with a crossplot in the λ-μ space. Without imposing petrophysical constraints, the $\lambda$ and $\mu$ values deviate from the true model as the similar radiation patterns of different model parameter perturbations result in crosstalk among physical properties. This problem is enlarged due to the limited acquisition coverage and varying illumination. The inversion does not recover the correct magnitude or size of the $\lambda$ model. Additionally, the $\mu$ model has a lot of artifacts due to the crosstalk between the elastic parameters. Although a linear relationship between the parameters characterizes the true model (Figure 3), the crossplot shown in Figure 4 indicates that the parameters $\lambda$ and $\mu$ are uncorrelated, which agrees with the fact that the data misfit objective function updates them independently, thus leading to unphysical models.

Based on the crossplot of true $\lambda$ and $\mu$ parameters (Figure 3), we choose the linear boundaries shown in Figure 5 to define the logarithmic penalty function. Adding the logarithmic penalty function $\mathcal{J}_L$ to $\mathcal{J}_D$ in the objective function, we obtain the $\lambda$ and $\mu$ models shown in Figure 6. The term $\mathcal{J}_L$ is not flat in the interval between the upper and lower boundaries and forces the recovered models toward a central region, as shown in Figure 6. The point (10.4, 5.2) GPa, which represents the background models, is not midway between the two boundaries; consequently, inversion using $\mathcal{J}_L$ changes the background parameters (Figure 6).

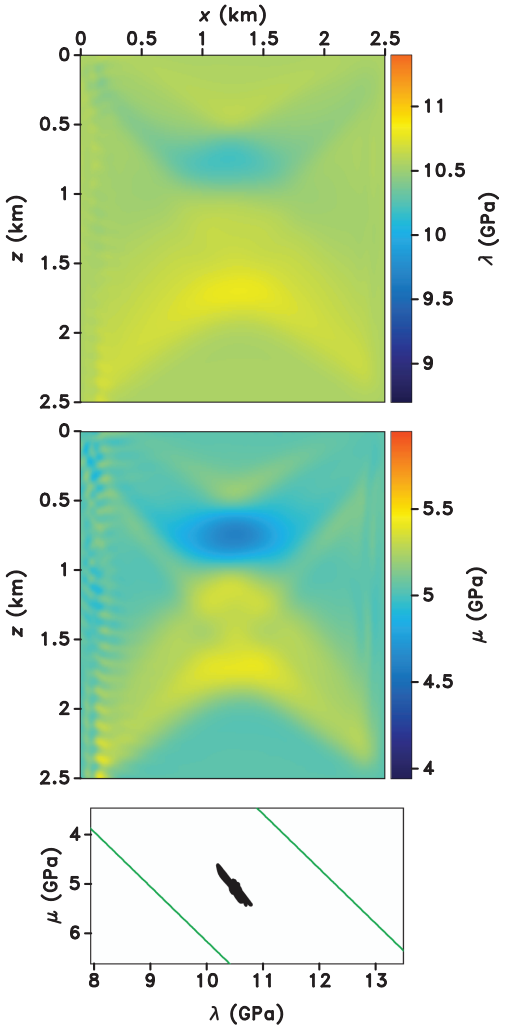


Figure 6. Updated $\lambda$ and $\mu$ models using the objective function $\mathcal{J}_D + \mathcal{J}_L$. The lines define the upper and lower boundaries used in the logarithmic penalty function $\mathcal{J}_L$. The Gaussian anomalies are not recovered well, and the backgrounds are modified during the inversion.

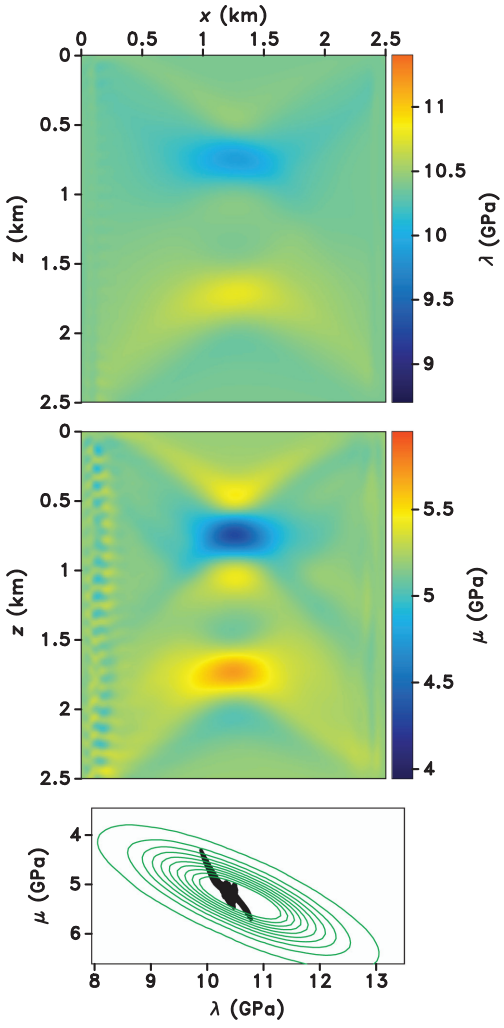


Figure 7. Updated $\lambda$ and $\mu$ models using the objective function $\mathcal{J}_D + \mathcal{J}_P$. The contours in the crossplot represent the PDF used to define the petrophysical constraint $\mathcal{J}_P$. Both Gaussian anomalies are better recovered for the $\lambda$ and $\mu$ models.

Downloaded 04/29/20 to 73.78.60.103. Redistribution subject to SEG license or copyright; see Terms of Use at http://library.seg.org/

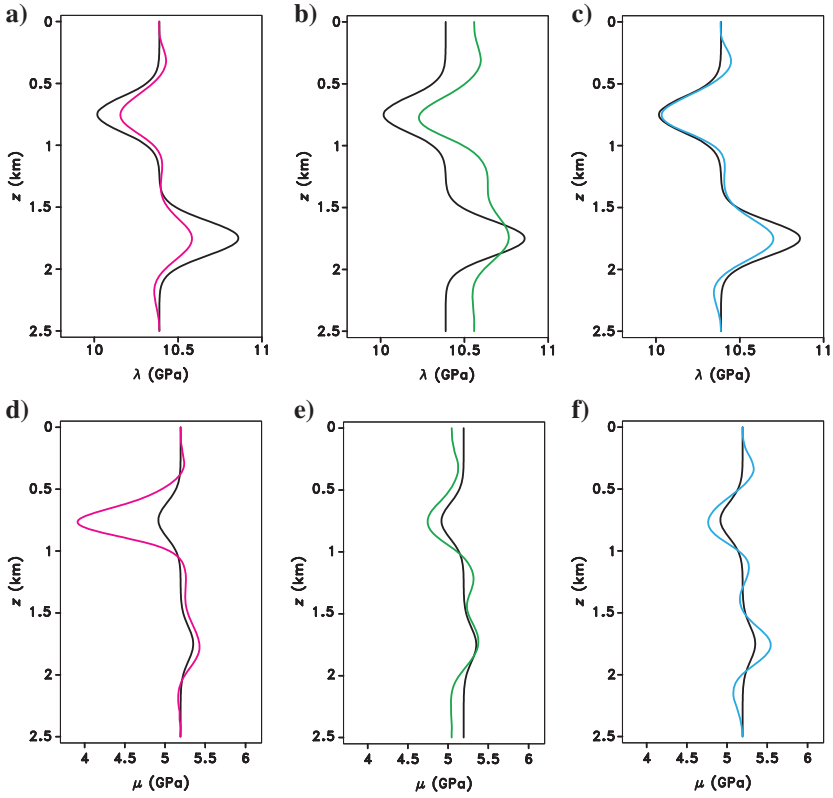


Figure 8. Comparison between true and recovered models in a vertical profile at $x = 1.0$ km. In the top row, the black lines are the true $\lambda$ model and the colored lines are the updated models using the objective functions (a) $\mathcal{J}_D$ (red line), (b) $\mathcal{J}_D + \mathcal{J}_L$ (green line), and (c) $\mathcal{J}_D + \mathcal{J}_P$ (blue line). In the bottom row, the black lines are the true $\mu$ model and the colored lines are the updated models using the objective functions (d) $\mathcal{J}_D$ (red line), (e) $\mathcal{J}_D + \mathcal{J}_L$ (green line), and (f) $\mathcal{J}_D + \mathcal{J}_P$ (blue line).

Figure 7 shows the recovered $\lambda$ and $\mu$ models using the objective function $\mathcal{J}_D + \mathcal{J}_P$. For simplicity, we define in this example the PDF as a Gaussian distribution covering the true model. This is not necessary for more complex examples, where the relationship between the parameters is nonlinear and is derived from actual well logs. The lines in the crossplot correspond to the feasible region used to define the probabilistic constraint $\mathcal{J}_P$. Notice that when we include the probabilistic constraint term both anomalies have an amplitude and shape closer to the true $\lambda$ and $\mu$ models (Figure 3). Imposing the probabilistic constraint confines the model to the feasible region defined by the PDF, but within this area the models do not follow any predefined trend, which does not happen when we use the logarithmic boundaries. Also, the crossplot shown in Figure 7 has two main linear relationships between the inverted models, what conforms to the true models.

Vertical profiles from the inverted $\lambda$ and $\mu$ models at $x = 1.0$ km are shown in Figure 8, where the black lines indicate the true models and the colored lines are the recovered models. Using the objective function $\mathcal{J}_D$, we obtain a reliable model update for $\lambda$ (Figure 8a), but an incorrect model update for $\mu$ (Figure 8d). Using the objective function $\mathcal{J}_D + \mathcal{J}_L$, we distort the background values and do not recover the anomalies (Figure 8b and 8e). Using the objective function $\mathcal{J}_D + \mathcal{J}_P$, we obtain models that better represent the true ones (Figure 8c and 8f), without negatively affecting the background model.

## Marmousi 2 model

The second synthetic example uses a portion of the Marmousi 2 model (Martin et al., 2002). For this example, we consider that prior petrophysical data from three well logs are available and we use this information to build the petrophysical model constraints. Figure 9 shows the correct $\lambda$ and $\mu$ models, the well locations for our experiment, and the crossplot of the model parameters. We simulate a multicomponent ocean-bottom seismic survey with a line of receiver at the water bottom ($z = 0.17$ km) and 20 evenly spaced pressure sources

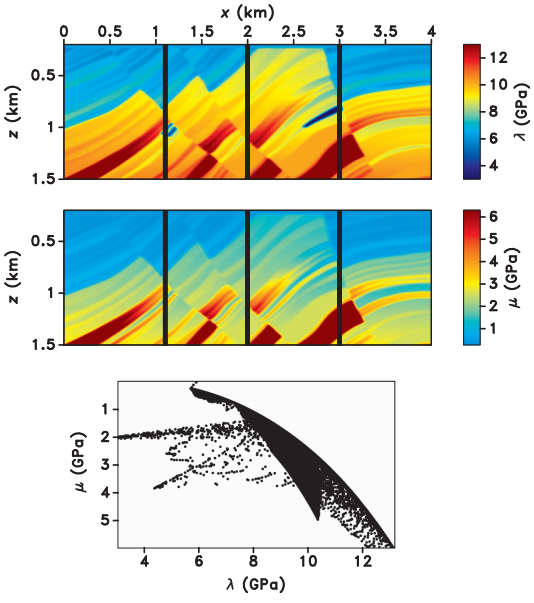


Figure 9. Marmousi 2 model: true $\lambda$ and $\mu$ models and their crossplot. The vertical lines correspond to the location of the wells, providing information for the petrophysical constraint.

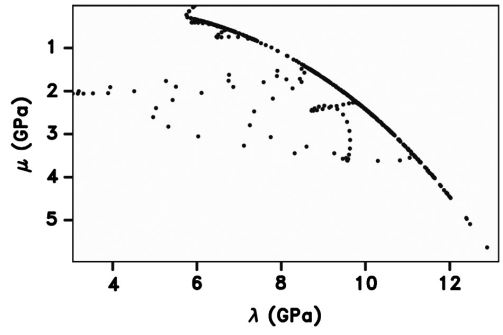


Figure 10. Crossplot of $\lambda$ and $\mu$ provided by the well logs indicated in Figure 9. The relationship between the model parameters is not linear and does not follow a simple trend.

Downloaded 04/29/20 to 73.78.60.103. Redistribution subject to SEG license or copyright; see Terms of Use at http://library.seg.org/

located at $z = 0.05$ km. Figure 10 shows the crossplot of the $\lambda$ and $\mu$ models extracted at the wells located at $x = 1.1$, 2.0, and 3.0 km (Figure 9). We use a 7.5 Hz peak Ricker source wavelet. Figure 11 shows the initial $\lambda$ and $\mu$ models and the corresponding crossplot in the model parameter space.

Figure 12 shows the recovered $\lambda$ and $\mu$ models using the objective function $\mathcal{J}_D$. As expected, the inverted $\mu$ model has more structural detail than the $\lambda$ model because it only depends on density and S-velocities, whereas $\lambda$ depends on density as well as the P- and S-velocities. The wavelength of the S-waves is shorter than that of the P-waves; therefore, the inverted $\mu$ model has higher spatial resolution. However, because in this example we do not impose petrophysical constraints, the $\mu$ model has spurious artifacts due to parameter crosstalk. Note that the values of the main structure presented in the initial $\lambda$ model (Figure 11) that conforms to the true $\lambda$ model (Figure 9) are not preserved during the unconstrained inversion (Figure 12). Additionally, the crossplot shown in Figure 12 does not resemble the true model (Figure 9) because the updates are not restricted to a feasible petrophysical region.

From the crossplot of the $\lambda$ and $\mu$ models extracted at the wells (Figure 10), we choose the linear boundaries shown in Figure 13 to estimate the logarithmic penalty function as $h_l = \lambda - 1.3\mu - 0.2$ and $h_u = -\lambda + 1.3\mu + 3.15$. Figure 14 shows the recovered $\lambda$ and $\mu$ models using the objective function $\mathcal{J}_D + \mathcal{J}_L$. We also ensure

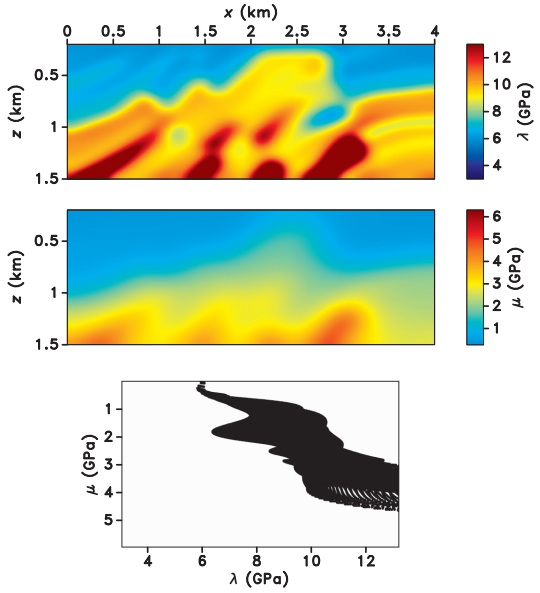


Figure 11. Marmousi 2 model: initial $\lambda$ and $\mu$ models and their crossplot in the $\lambda$-$\mu$ space.

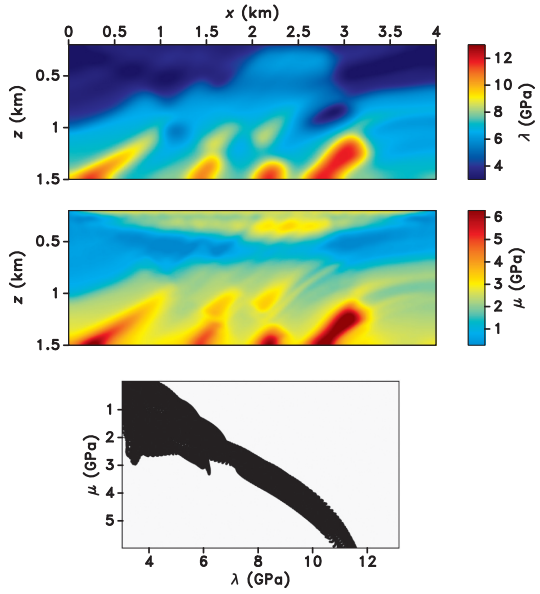


Figure 12. Marmousi 2 model: recovered $\lambda$ and $\mu$ models using objective function $\mathcal{J}_D$. The inverted $\mu$ model has more structural details than the $\lambda$ model.

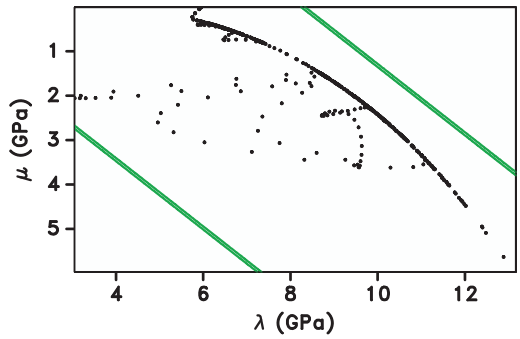


Figure 13. Crossplot of the $\lambda$ and $\mu$ parameters extracted at the well location, superimposed by the upper and lower boundaries used in the logarithmic penalty function $\mathcal{J}_L$. As in the Gaussian example (Figure 5), the linear barriers ensure that the inversion recovers models confined to this feasible region.

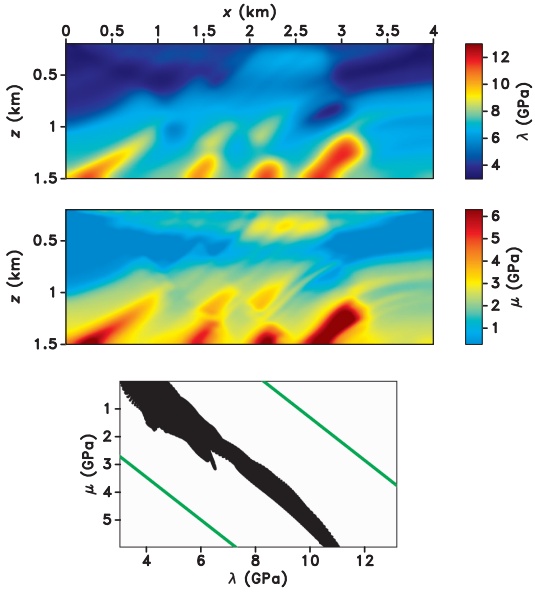


Figure 14. Marmousi 2 model: recovered $\lambda$ and $\mu$ models using objective function $\mathcal{J}_D + \mathcal{J}_L$. The lines in the crossplot define the upper and lower boundaries used in the logarithmic penalty function $\mathcal{J}_L$. The inverted model is forced to be in the middle area of the feasible region, which does not reflect correctly the trend shown in Figure 9 for the true model.

Downloaded 04/29/20 to 73.78.60.103. Redistribution subject to SEG license or copyright; see Terms of Use at http://library.seg.org/

that initial models for the inversion (Figure 11) are within the feasible region. As for the case of inversion using the objective function $\mathcal{J}_D$ (Figure 12), the inverted $\mu$ model has spurious artifacts. The main structure presented in the initial $\lambda$ model (Figure 11) is not preserved during this kind of constrained inversion (Figure 14).

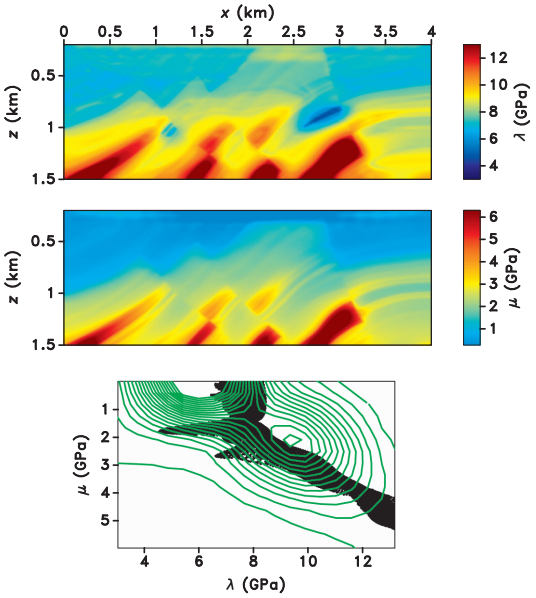


Figure 15. Marmousi 2 model: recovered $\lambda$ and $\mu$ models using objective function $\mathcal{J}_D + \mathcal{J}_P$ with $a = 5 \times 10^{-8}$. The contours in the crossplot represent the feasible area for the probabilistic constraint $\mathcal{J}_P$. The probabilistic petrophysical constraint leads to better recovered models than the unconstrained inversion (Figure 12) or the inversion with approximate analytic constraints (Figure 14).

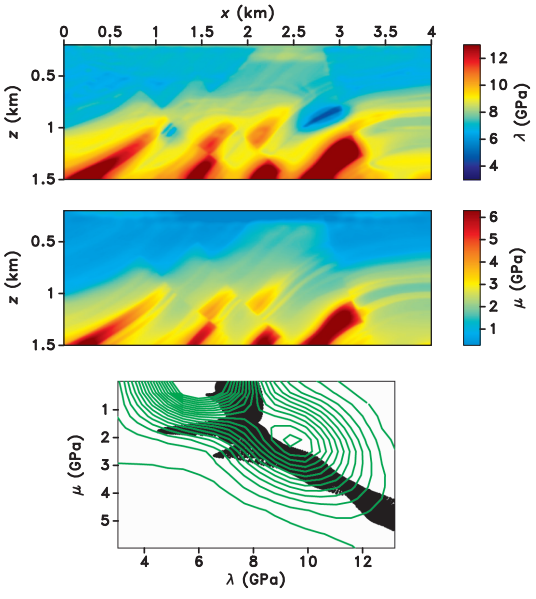


Figure 16. Marmousi 2 model: recovered $\lambda$ and $\mu$ models using objective function $\mathcal{J}_D + \mathcal{J}_P$ with $a = 3 \times 10^{-8}$. These recovered models are very similar to the ones shown in Figure 15, where $a = 5 \times 10^{-8}$.

As expected, the crossplot shown in Figure 14 indicates that the model samples follow the linear trend imposed by the barriers. However, this trend does not correspond to the true models (Figure 9).

Figures 15, 16, and 17 show the recovered $\lambda$ and $\mu$ models using the objective function $\mathcal{J}_D + \mathcal{J}_P$ with $a$ equal to, respectively, $5 \times 10^{-8}$, $3 \times 10^{-8}$, and $10^{-9}$. We estimate the PDF presented in the crossplots as the contour lines from the well-log data, but without user-defined parameters. The terms $\lambda$ and $\mu$ models in Figures 15–17 present similar resolution and are better recovered compared with the cases when we use the objective functions $\mathcal{J}_D$ (Figure 12) or $\mathcal{J}_D + \mathcal{J}_L$ (Figure 14). Additionally, the $\mu$ model artifacts are attenuated when we incorporate the probabilistic petrophysical constraints in the inversion. Also, the crossplot built with the inverted models (Figures 15–17) is closer to the similar crossplot built with the correct model parameters relative to the crossplots obtained for the less robust objective functions $\mathcal{J}_D$ (Figure 12) or $\mathcal{J}_D + \mathcal{J}_L$ (Figure 14). When comparing the recovered models shown in Figures 15–17, one can see that when $a = 10^{-9}$ (Figure 17) the inversion does not recover such accurate and feasible models as when $a = 5 \times 10^{-8}$ (Figure 15) or $a = 3 \times 10^{-8}$ (Figure 16). Therefore, when we reduce the strength of the $\mathcal{J}_P$ term, the quality of the recovered models is compromised because the artifacts in the $\mu$ model located in the shallow depths, for example, are better attenuated when $a = 5 \times 10^{-8}$ (Figure 15) or $a = 3 \times 10^{-8}$ (Figure 16) than when $a = 10^{-9}$ (Figure 17).

## DISCUSSION

The quality of elastic models derived from seismic wavefield tomography is often poor because the inversion is nonlinear and ill-posed, and the objective function is nonconvex. Thus, the inversion may converge to a local minimum due to the lack of access to

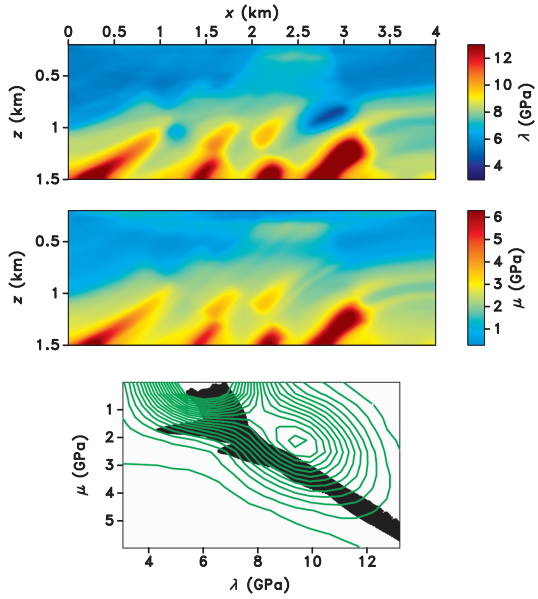


Figure 17. Marmousi 2 model: recovered $\lambda$ and $\mu$ models using objective function $\mathcal{J}_D + \mathcal{J}_P$ with $a = 10^{-9}$. Because we use a smaller $a$ than in the previous examples, the impact of the petrophysical penalty term in the object function is greatly reduced, which leads to poor recovered models compared with the ones shown in Figures 15 and 16 where $a$ is equal to, respectively, $5 \times 10^{-8}$ and $3 \times 10^{-8}$.

Downloaded 04/29/20 to 73.78.60.103. Redistribution subject to SEG license or copyright; see Terms of Use at http://library.seg.org/

good starting models, data noise and modeling errors, the absence of low frequencies in the data, incomplete acquisition coverage, and the dimensionality of the model space. Additionally, simultaneous determination of multiple physical parameters using FWI suffers from interparameter trade-offs and model updates provided by this methodology may not represent real lithologies in unconstrained multiparameter inversion. A well-known approach to counter these deficiencies is to include model regularization in the inversion, which mitigates the ill-posedness and nonuniqueness of the inverse problem. Although regularization methods have enabled enormous progress in ill-posed geophysical inverse problems, they can guide inversion toward models that do not truly represent the subsurface, when accurate geologic information about the entire studied region is not available. Petrophysical information provided by well logs or other sources describes the model only at sparse locations; therefore, well-log information cannot easily form the basis of model regularization in the space domain.

The technique we present in this study does not rely on accurate prior information about the whole investigated area. Instead, it uses petrophysical information in the model parameter domain without assuming any specific analytic relationship among the different elastic parameters. Such technique prevents incorrect model updates in regions where seismic data are inefficient and do not constrain sufficiently the subsurface properties. This technique addresses many relevant problems of EFWI. By incorporating prior information into the inversion, we reduce the number of possible model solutions and improve the inversion convergence toward the global minimum. Additionally, by linking the elastic parameters during the inversion, we can avoid geologically implausible earth models and mitigate the artifacts created by interparameter crosstalk. From the synthetic examples that we present in this study, one can see that the use of the probabilistic petrophysical penalty term also mitigates the potentially deleterious effects of the source radiation pattern and of limited acquisition aperture. Thus, the methodology outlined here would establish a more robust foundation for FWI by explicitly guiding models toward plausible solutions in the specific geologic context of the exploration problem. FWI augmented with petrophysical information would define a higher standard for estimating high-resolution, accurate, and lithologically feasible subsurface models in land and marine environments.

An alternative to further enhance the geologic model realism is given by imposing a model regularization term in addition to petrophysical model constraints. Petrophysical constraints are complementary to spatial regularization and confine model updates to realistic combinations that represent the known geologic context in the investigated area.

## CONCLUSION

We incorporate petrophysical information into the EFWI, using PDFs derived from information provided by well logs or from other forms of rock-physics analysis. We demonstrate that imposing petrophysical constraints in elastic wavefield tomography improves the quality of the recovered models, by restricting them to a feasible region, therefore guiding the inversion toward geologically plausible solutions. Two synthetic examples show that the models recovered with the proposed method are closer to the true models, while maintaining robust and realistic petrophysical relationships between the model parameters. This constraint term also helps mitigate the interparameter crosstalk created by similar radiation patterns among the elastic parameters.

## ACKNOWLEDGMENTS

We acknowledge the Coordination of Improvement of Higher Education Personnel — Brazil (CAPES) for financial support (Finance Code 001). We thank the sponsors of the Center for Wave Phenomena for the additional support of this research. The synthetic examples in this paper use the Madagascar open-source software package (Fomel et al., 2013) freely available from http://www.ahay.org.

## DATA AND MATERIALS AVAILABILITY

Data associated with this research are available and can be obtained by contacting the corresponding author.

## REFERENCES

Alkhalifah, T., and Y. Choi, 2014, From tomography to FWI with a single objective function: Geophysics, **79**, no. 2, R55–R61, doi: 10.1190/geo2013-0291.1.

Aragao, O., and P. Sava, 2019, Elastic full waveform inversion with probabilistic petrophysical model constraints: 89th Annual International Meeting, SEG, Expanded Abstracts, 1425–1429, doi: 10.1190/segam2019-3215944.1.

Asnaashari, A., R. Brossier, S. Garambois, F. Audebert, P. Thore, and J. Virieux, 2013, Regularized seismic full waveform inversion with prior model information: Geophysics, **78**, no. 2, R25–R36, doi: 10.1190/geo2012-0104.1.

Baumstein, A., 2013, POCS-based geophysical constraints in multiparameter full wavefield inversion: 75th Annual International Conference and Exhibition, EAGE, Extended Abstracts, doi: 10.3997/2214-4609.20130409.

Biondi, B., 2006, 3D seismic imaging: SEG.

Diaz, E., and P. Sava, 2017, Cascaded wavefield tomography and inversion using extended common-image-point gathers: A case study: Geophysics, **82**, no. 5, S391–S401, doi: 10.1190/geo2016-0318.1.

Djebbi, R., and T. Alkhalifah, 2018, Frequency domain multi-parameter acoustic inversion for transversely isotropic media with a vertical axis of symmetry: Geophysics, **84**, no. 1, C1–C14, doi: 10.1190/geo2017-0564.1.

Duan, Y., and P. Sava, 2016, Elastic wavefield tomography with physical model constraints: Geophysics, **81**, no. 6, R447–R456, doi: 10.1190/geo2015-0508.1.

Fomel, S., P. Sava, I. Vlad, Y. Liu, and V. Bashkardin, 2013, Madagascar: Open-source software project for multidimensional data analysis and reproducible computational experiments: Journal of Open Research Software, **1**, e8, doi: 10.5334/jors.ag.

Jun, H., J. Kwon, C. Shin, H. Zhou, and M. Cogan, 2017, Regularized Laplace-Fourier-domain full waveform inversion using a weighted L-2 objective function: Pure and Applied Geophysics, **174**, 955–980, doi: 10.1007/s00024-016-1398-5.

Kamath, N., and I. Tsvankin, 2016, Elastic full-waveform inversion for VTI media: Methodology and sensitivity analysis: Geophysics, **81**, no. 2, C53–C68, doi: 10.1190/geo2014-0586.1.

Manukyan, E., H. Maurer, and A. Nuber, 2018, Improvements to elastic full-waveform inversion using cross-gradient constraints: Geophysics, **83**, no. 2, R105–R115, doi: 10.1190/geo2017-0266.1.

Martin, G., K. Marfut, and S. Larsen, 2002, Marmousi-2: An updated model for the investigation of AVO in structurally complex areas: 72nd Annual International Meeting, SEG, Expanded Abstracts, 1979–1982, doi: 10.1190/1.1817083.

Masmoudi, N., and T. Alkhalifah, 2018, Full waveform inversion in acoustic orthorhombic media and application to a North Sea data set: Geophysics, **83**, no. 5, C179–C193, doi: 10.1190/geo2017-0738.1.

Mora, P., 1989, Inversion = migration + tomography: Geophysics, **54**, 1575–1586, doi: 10.1190/1.1442625.

Oh, J., M. Kalita, and T. Alkhalifah, 2018, 3D elastic full waveform inversion using P-wave excitation amplitude: Application to real OBC data: Geophysics, **83**, no. 2, R129–R140, doi: 10.1190/geo2017-0236.1.

Operto, S., Y. Gholami, V. Prieux, A. Ribodetti, R. Brossier, L. Metivier, and J. Virieux, 2013, A guided tour of multiparameter full-waveform inversion with multicomponent data: From theory to practice: The Leading Edge, **32**, 1040–1054, doi: 10.1190/tle32091040.1.

Plessix, R. E., 2006, A review of the adjoint-state method for computing the gradient of a functional with geophysical applications: Geophysical Journal International, **167**, 495–503, doi: 10.1111/j.1365-246X.2006.02978.x.

Pratt, R. G., 1990, Inverse theory applied to multi-source cross-hole tomography: Geophysical Prospecting, **38**, 311–329, doi: 10.1111/j.1365-2478.1990.tb01847.x.

Pratt, R. G., 1999, Seismic waveform inversion in the frequency domain — Part 1: Theory and verification in a physical scale model: Geophysics, **64**, 888–901, doi: 10.1190/1.1444597.

Pratt, R. G., Z. M. Williamson, and M. Warner, 1996, Two-dimensional velocity model from wide-angle seismic data by wavefield inversion: Geophysical Journal International, **124**, 323–340, doi: 10.1111/j.1365-246X.1996.tb07023.x.

Rocha, D., and P. Sava, 2018, Elastic-reflection waveform inversion with petrophysical model constraints: 88th Annual International Meeting, SEG, Expanded Abstracts, 1203–1207, doi: 10.1190/segam2018-2997220.1.

Schuster, G. T., and A. Quintus-Bosz, 1993, Wavepath Eikonal traveltime inversion: Theory: Geophysics, **58**, 1314–1323, doi: 10.1190/1.1443514.

Sirgue, L., and R. Pratt, 2004, Efficient waveform inversion and imaging: A strategy for selecting temporal frequencies: Geophysics, **69**, 231–248, doi: 10.1190/1.1649391.

Symes, W. W., 2008, Migration velocity analysis and waveform inversion: Geophysical Prospecting, **56**, 765–790, doi: 10.1111/j.1365-2478.2008.00698.x.

Taillandier, C. M., M. Noble, H. Chauris, and H. Calandra, 2009, First-arrival traveltime tomography based on the adjoint-state method: Geophysics, **74**, no. 6, WCB1–WCB10, doi: 10.1190/1.3250266.

Tarantola, A., 1984, Inversion of seismic reflection data in the acoustic approximation: Geophysics, **49**, 1259–1266, doi: 10.1190/1.1441754.

Tarantola, A., 1986, A strategy for nonlinear elastic inversion of seismic reflection data: Geophysics, **51**, 1893–1903, doi: 10.1190/1.1442046.

Tarantola, A., 1988, Theoretical background for the inversion of seismic waveforms including elasticity and attenuation: Pure and Applied Geophysics, **128**, 365–399, doi: 10.1007/BF01772605.

Tarantola, A., 2005, Inverse problem theory and methods for model parameter estimation: SIAM.

Tikhonov, A., and V. Arsenin, 1977, Solution of ill-posed problems: Winston and Sons.

Virieux, J., and S. Operto, 2009, An overview of full-waveform inversion in exploration geophysics: Geophysics, **74**, no. 6, WCC1–WCC26, doi: 10.1190/1.3238367.

Woodward, M. J., 1992, Wave-equation tomography: Geophysics, **57**, 15–26, doi: 10.1190/1.1443179.

Zhang, Z., and T. Alkhalifah, 2019, Regularized elastic full-waveform inversion using deep learning: Geophysics, **84**, no. 5, R741–R751, doi: 10.1190/geo2018-0685.1.

Zhang, Z., T. Alkhalifah, E. Z. Naeini, and B. Sun, 2018, Multiparameter elastic full wave form inversion with facies-based constraints: Geophysical Journal International, **213**, 2112–2127, doi: 10.1093/gji/ggy113.

Zhang, Z., T. Alkhalifah, Z. Wu, Y. Liu, B. He, and J. Oh, 2019, Normalized nonzero-lag crosscorrelation elastic full waveform inversion: Geophysics, **84**, no. 1, R1–R10, doi: 10.1190/geo2018-0082.1.

Downloaded 04/29/20 to 73.78.60.103. Redistribution subject to SEG license or copyright; see Terms of Use at http://library.seg.org/